

# **Nanometer resolved single-molecule colocalization of nuclear factors by two-color super resolution microscopy imaging**

*Mariya Georgieva, Diego I. Cattoni, Jean-Bernard Fiche, Thibaut Mutin, Delphine Chamousset and Marcelo Nollmann<sup>#</sup>*

Centre de Biochimie Structurale, CNRS UMR5048, INSERM U1054, Université de Montpellier, 29 rue de Navacelles, 34090 Montpellier, France

<sup>#</sup> To whom correspondence should be addressed: [marcelo.nollmann@cbs.cnrs.fr](mailto:marcelo.nollmann@cbs.cnrs.fr)

## **Keywords**

Protein-DNA interactions, Stochastic optical reconstruction microscopy (STORM), Photo-activated localization microscopy (PALM), Image analysis, *Drosophila*, colocalization quantification.

## Abstract

In order to study the detailed assembly and regulation mechanisms of complex structures and machineries in the cell, simultaneous *in situ* observation of all the individual interacting components should be achieved. Multi-color Single-Molecule Localization Microscopy (SMLM) is ideally suited for these quantifications. Here, we build on previous developments and thoroughly discuss a protocol for two-color SMLM combining PALM and STORM, including sample preparation details, image acquisition and data postprocessing analysis. We implement and evaluate a recently proposed colocalization analysis method (aCBC) that allows single-molecule colocalization quantification with the potential of revealing fine, nanometer-scaled, structural details of multicomponent complexes. Finally, using a doubly-labeled nuclear factor (Beaf-32) in *Drosophila* S2 cells we experimentally validate the colocalization quantification algorithm, highlight its advantages and discuss how using high molecular weight fluorescently labeled tags compromises colocalization precision in two-color SMLM experiments.

## 1. Introduction

DNA–protein interactions mediate a vast amount of cellular processes. At the nuclear level they control essential DNA processes (e.g. DNA transcription, repair and segregation) and at the whole cell they can regulate complex interaction networks controlling, among others, cell cycle, metabolism and homeostasis. In particular, chromatin remodelers and the transcription machinery are essential players in the regulation of gene expression. A large set of approaches have been developed to study the mechanisms of protein-protein and protein-DNA interactions in the nucleus. Two main limitations arise when employing some of the most widely extended approaches. On the one hand, *in vivo* high-throughput technologies (e.g. bacterial one-hybrid, DNase footprint, chromatin immunoprecipitation, luminescence technologies, chromosome conformation capture [1,2]) average population information and hinder access to the single-cell dynamics. On the other hand, *in vitro* bulk, single-molecule and structural studies (e.g. electrophoretic mobility shift assay, fluorescence anisotropy, stop-flow, atomic force microscopy, optical and magnetic tweezers, X-ray crystallography, Nuclear Magnetic Resonance and Electron Tomography [3,4]) study the interacting partners outside the cellular context in which additional elements can play specific and perhaps essential roles (e.g. molecular crowding, presence of known or unknown partners).

*In vivo* fluorescence microscopy overcomes the above mentioned limitations and enables the non-invasive observation of protein organization and localization in live cells with high specificity. Multicolor fluorescence imaging of cellular components has the potential to reveal spatial proximity (colocalization) of the labeled species. To study molecular interactions on the <10 nm length scale Förster Resonance Energy Transfer (FRET) techniques are most commonly applied [5]. At larger distances, the colocalization or the degree of spatial coincidence between the molecular species of interest are estimated in a qualitative or quantitative manner using diffraction-limited microscopies [6]. However, the sensitivity of this colocalization strategies is limited by the maximum resolution attainable in standard fluorescence microscopy (~ 250 nm) and by the fact that the fluorescence signal collected will arise from a population of molecules emitting simultaneously within the diffraction-limited volume, averaging the heterogeneity and dynamics of protein-protein and protein-DNA interactions.

Over the past decade, several subdiffraction resolution imaging techniques have undergone remarkable developments in instrumentation and analytical tools, which allow the investigation of nanometer-sized cellular components. The three main approaches are known as Structured Illumination Microscopy (SIM), Stimulated Emission Depletion Microscopy (STED) and Single-Molecule Localization Microscopy (SMLM) [7–9]. SMLM methods combine the stochastic photoactivation of a single fluorophore per diffraction-limited volume at any given time and its spatial localization with nanometer precision. From the coordinates of all localized emitters, a reconstructed image at super-resolution (~20-30 nm) can be obtained. Several SMLM strategies have been designed differing mostly in the fluorescent probe employed and the mechanism for achieving stochastic photoactivation, with Photo-activated localization microscopy

(PALM/fPALM) and Stochastic Optical Reconstruction Microscopy (STORM/dSTORM) being the most widely applied methods [10–14]. So far, these technologies have revealed novel properties of various subcellular structures and machineries. Hence, combining multi-color labelling with SMLM imaging should allow the simultaneous observation, at the single-molecule level, of two or more components in molecular assemblies, revealing mechanistic and regulatory aspects that so far remain unattainable. The number of probes to perform efficient multi-color labelling in SMLM experiments is limiting mostly due to spectral overlap, particularly when it comes to genetically encoded probes [15,16]. Successful strategies have proven the potential of two-color imaging using both photoactivatable proteins [17–20] and single [21,22] or multiple [23–25] synthetic fluorophores. However, despite its great potential, multi-color SMLM methodologies are yet to spread amongst the biological community, possibly due to limitations in the implementation of these complex technologies. In particular, the existing bibliography is limited on practical aspects of SMLM, such as stringent protocols for sample preservation and highest labeling density, detailed imaging conditions and thorough data interpretation.

In this article, we build on previous developments and implement an improved protocol for two-color SMLM using PALM/dSTORM. We describe thoroughly sample preparation, cell fixation strategies, antibody labeling for dSTORM as well as setup and software adaptations for optimal imaging. We propose a detailed pipeline to perform sequential two-color SMLM imaging and discuss acquisition conditions, data post-processing including single molecule localization, chromatic and drift-related corrections, image segmentation and final image reconstruction. We discuss in detail the implementation of a new algorithm (aCBC) using a statistical estimator of the colocalization between two molecular species and perform a wide set of simulated SMLM datasets to evaluate the robustness and reproducibility of the method. We also thoroughly explore aCBC input space-parameter values to define optimal colocalization criteria and quantification according to structural properties of the observed molecular species. Finally, employing as a validation model a double labeled nuclear protein (Beaf-32) in *Drosophila melanogaster* (*D. melanogaster*) cells, we experimentally evaluate the performance of the colocalization analysis and highlight the advantages of primary over secondary antibody labeling to increase the colocalization precision results in two-color SMLM.

## 2. Materials and Methods

### 2.1. Sample preparation

The protocol discussed in this section provides key steps for sample fixation and labeling for multicolor SMLM imaging of nuclear structures in *Drosophila* cells. The sample preparation conditions have been optimized to yield the highest labeling specificity and fluorescent signal. Sample particularities such as cell type, cell compartment and target molecule were taken into account and several protocols were evaluated as discussed for instance in [26,27]. Note that the handling and seeding of cells presented below can also be performed on non- or semi-adherent mammalian cell lines. All materials employed in this work were of analytical grade. All steps are to be carried out at room temperature unless otherwise indicated.

#### 2.1.1. Cell culture and transfection with Beaf-32-mEos2

*Drosophila* S2 cells were grown in Schneider's *Drosophila* medium (Gibco) in cell culture flasks (Nunc) supplemented with 10% fetal bovine serum at 25°C. The mEos2-Beaf-32 sequence was synthesized by Clontech before cloning into the plasmid pMT/V5-His-TOPO (DES TOPO TA Expression kit, LifeTechnologies) and used for the following transfection protocol. Transfections were performed in S2 cells that were plated at 2 million cells per well in a 6-well plate containing 2 ml of Schneider's medium per well. Cells were incubated for 2-3h at 25°C and transfected with Effectene reagent (Qiagen) in a mix containing 100 µl EC buffer, 0.4 µg pMT/V5-His-TOPO mEos2-Beaf-32, 3.2 µl enhancer, 20 µl Effectene. After 24h, copper sulfate CuSO<sub>4</sub> (250 µM) was added to activate the *Drosophila* metallothionein (MT) promoter for metal-inducible expression of the Beaf-32 gene. The day after (i.e. 48h after the transfection), cells were harvested.

#### 2.1.2. Cell fixation and permeabilization

S2 cells were fixed with 4% PFA (Electron microscopy sciences) for 15 min at room temperature (RT) and next washed three times with Phosphate-buffered saline solution (PBS) for 5 min at RT. Next, plasma and nuclear membranes were permeabilized with Triton X-100 (Sigma) 0.5% for 5 min at RT and washed three times with PBS for 5 min at RT. To ensure reproducibility, all solutions are made fresh prior to each labeling experiment.

#### 2.1.3. Affinity staining of nuclear proteins using antibodies (Immunofluorescence)

After permeabilization, nonspecific antibody binding sites were blocked with 10% bovine serum albumin (BSA) at RT for at least 1h. Next, S2 cells were incubated with custom-raised rabbit antibodies

directed against Beaf-32 (Eurogentec) at a concentration of 5 µg/ml at 4°C for 12-16 h followed by three PBS washes. For direct immunofluorescence experiments, anti-Beaf-32 antibodies (primary antibodies) were coupled to Alexa Fluor 647 (AF647, Molecular Probes, Invitrogen) at an average density of 1-1.5 fluorophores per antibody molecule. For indirect immunofluorescence, AF647 coupling was performed on goat anti-rabbit Fab2 antibody fragments (secondary antibodies, Jackson ImmunoResearch) instead of on primary antibodies. Secondary antibody incubation was performed subsequently to unlabeled primary antibodies at a concentration of 5 µg/ml at 4°C for 12-16 h preceded and followed by three PBS washes.

Antibodies were validated and their concentrations were determined to ensure for the best labeling density in SMLM experiments with minimal nonspecific labeling. Control experiments were performed to validate specificity of primary antibodies using RNAi and that of secondary antibodies through a negative control without primary antibody incubation, as discussed in [28,29].

Custom fluorescent labeling of affinity-purified antibodies (at a concentration >2mg/ml) with the desired fluorophore to antibody molecular ratios was performed in PBS (pH 7.4) at RT for 1h30. The amount of AF647 succinimidyl ester added was calculated to obtain a antibody:fluorophore mass ratio of 30:1. The labeling reaction was stopped with 10 mM final concentration of Tris pH7.5. Unreacted dye molecules were discarded using dialysis.

#### 2.1.4. Cell seeding for microscopy

After discarding floating and dead cells, cells were gently detached from the recipient's surface with the help of a cell scraper (Nunc) and concentrated by centrifugation at 900 rpm for 3 minutes at 25°C and subsequently resuspended in 2-3 ml of culture medium. Next, 200 µl of the cell suspension was deposited on coverslips coated with Poly-L-Lysine (neuVibro). The seeded cells were then allowed to adhere for 1h at 25°C. Typically this procedure yields a 50-70 % of cell confluence per field of view (FOV) which allows imaging of ~5-10 cells simultaneously per acquisition.

#### 2.1.5. Sample mounting

After 3 final PBS washes, 0.1 µm fluorescent beads emitting at four wavelengths (TetraSpeck Microspheres, Invitrogen) used as fiducial marks were incubated at 1/1500 dilution with cells for 5 min under horizontal rotation. Immediately after, samples were mounted for SMLM imaging in 100 µl of photoswitching buffer on a microscope well slide. The buffer cocktail employed to induce photoswitching of organic fluorophores in dSTORM was a modified variant of the frequently used enzyme-based oxygen scavenging system in combination with a thiol as a reducer [10], composed of PBS; 2.5 mg/ml glucose oxidase (Sigma); 0.2 mg/ml catalase (Sigma); 10% glucose; 50 mM of β-mercaptoethylamine (MEA). To isolate the mounting medium from ambient oxygen, the sample was sealed with duplicating silicone (Rotec).

## 2.2. Instrumentation and Imaging

SMLM experiments were carried out in a custom-made inverted microscope with an oil-immersion objective (Plan-Apocromat, 100x, 1.4NA oil DIC, Zeiss) mounted on a z-axis piezoelectric stage (P-721.CDQ, PICOPI, PI). A 1.5x telescope was used to obtain a final imaging magnification of 150-fold corresponding to a pixel size of 105 nm. Three lasers were used for excitation/photo-activation: 405 nm (OBIS, LX 405-50, Coherent Inc.), 488 nm (OBIS, LX 488-50, Coherent Inc.), 561 nm (OBIS, LX 561-50, Coherent Inc.), and 640 nm (OBIS, LX 640-100, Coherent Inc.). Laser lines were expanded, and coupled into a single beam using dichroic mirrors (427, 552 and 613 nm Laser MUX<sup>TM</sup>, Semrock). An acousto-optic tunable filter (AOTFnc-400.650-TN, AA opto-electronics) was used as to modulate laser intensity. Light was circularly polarized using an achromatic quarter wave plate (QWP). Two achromatic lenses were used to expand the excitation laser and an additional dichroic mirror (zt405/488/561/638rpc, Chroma) to direct it towards the back focal plane of the objective. Fluorescence light was spectrally filtered with emission filters (ET525/50m, ET600/50m and ET700/75m, Chroma Technology) and imaged on an EMCCD camera (iXon X3 DU-897, Andor Technologies). The microscope was equipped with a motorized stage (MS-2000, ASI) to translate the sample perpendicularly to the optical axis. To ensure the stability of the focus during the acquisition, a home-made autofocus system was built. A 785 nm laser beam (OBIS, LX 785-50, Coherent Inc.) was expanded twice and directed towards the objective lens by a dichroic mirror (zt1064rdc-sp, Chroma). The reflected IR beam was redirected following the same path as the incident beam and guided to a CCD detector (Pixelfly, Cooke) by a polarized beam splitter cube (PBS). Camera, lasers and filter wheel were controlled with software written in Labview [30].

Lateral drift correction was performed by following the trajectory of fiducial marks and employing an algorithm previously described [31]. The experimental drift correction precision was typically 3-10 nm. Lower precision experiments were typically discarded.

For image acquisition, on average 30,000 frames (per detection channel in two-color acquisitions) were recorded at a rate of 50 ms/frame. Continuous excitation and activation was employed for all fluorophores employed in this work with powers as follows: 1 kW/cm<sup>2</sup> at 641 nm (for AF647), 0.8-1.2 kW/cm<sup>2</sup> at 561 nm (for mEos2), and 0-0.1 kW/cm<sup>2</sup> at 405 nm for activation. The intensity of activation was progressively increased throughout the acquisition to ensure a constant amount of simultaneously emitting fluorophores within the labeled structures.

## 2.3. Automated Coordinate-based colocalization analysis (aCBC)

We implemented an automatic single-molecule colocalization quantification algorithm based on Coordinate-Based Colocalization (CBC) [32]. This automated methodology (that we coin aCBC) was applied to evaluate protein proximity *in vivo* by SMLM (see sections 5 and 6). In CBC, a colocalization coefficient is



attributed to each single-molecule localization, from each detection channel, by calculating the Spearman rank-order correlation. If  $A$  are all events detected in the first channel and  $B$  are all events detected in the second channel, then the CBC coefficient of the localization  $A_i$  is determined as follows [32]:

First, the distribution of localizations of species  $A$  around  $A_i$  is calculated as:

$$D_{A_i, A}(r) = \frac{N_{A_i, A}(r)}{\pi r^2} \cdot \frac{\pi R_{max}^2}{N_{A_i, A}(R_{max})} = \frac{N_{A_i, A}(r)}{N_{A_i, A}(R_{max})} \cdot \frac{R_{max}^2}{r^2} \quad \text{Eq.1}$$

Second, the distribution of localizations of species  $B$  around  $A_i$  is calculated as:

$$D_{A_i, B}(r) = \frac{N_{A_i, B}(r)}{N_{A_i, B}(R_{max})} \cdot \frac{R_{max}^2}{r^2} \quad \text{Eq.2}$$

where  $N_{A_i, A}(r)$  is the number of localizations of species  $A$  within the distance  $r$  around  $A_i$ , and  $N_{A_i, B}(r)$  is the number of localizations of species  $B$  within the distance  $r$  around  $A_i$ . The distributions are corrected for the area ( $\pi r^2$ ), normalized by the number of localizations within the largest observed distance  $R_{max}$  and divided by the largest observed area for species  $A$  ( $N_{A_i, A}(R_{max})/\pi R_{max}^2$ ) and  $B$  ( $N_{A_i, B}(R_{max})/\pi R_{max}^2$ ). A uniform distribution would give an expected value of  $D(r) = 1$  for all  $r$ . Next, ranks are attributed to each distribution of  $r$  and the Spearman rank correlation for each event is obtained.

$$S_{A_i} = \frac{\sum_{r_j=0}^{R_{max}} (OD_{A_i, A}(r_j) - \overline{OD_{A_i, A}})(OD_{A_i, B}(r_j) - \overline{OD_{A_i, B}})}{\sqrt{\sum_{r_j=0}^{R_{max}} (OD_{A_i, A}(r_j) - \overline{OD_{A_i, A}})^2} \sqrt{\sum_{r_j=0}^{R_{max}} (OD_{A_i, B}(r_j) - \overline{OD_{A_i, B}})^2}} \quad \text{Eq.3}$$

where  $OD_{A_i, A}(r)$  is the rank of  $D_{A_i, A}(r)$  calculated after Spearman, and  $\overline{OD_{A_i, A}}$  is the arithmetic average of  $OD_{A_i, A}(r)$ . Finally, the colocalization value ( $CA_i$ ), is calculated as:

$$C_{A_i} = S_{A_i} \cdot e^{(-\frac{E_{A_i, B}}{R_{max}})} \quad \text{Eq.4}$$

where  $EA_{i,B}$  is the distance from  $A_i$  to the nearest neighbor from species B.  $CA_i$  is computed for every single-molecule localization and can take values from  $-1$  to  $1$ , similarly to the Pearson coefficient employed for colocalization analysis of conventional two-color microscopy images.

In automated CBC (aCBC),  $r$  and  $Rmax$  values were user-defined, such that the former corresponds to the distance distribution binning size and the latter, defines the maximal area, in which correlation is probed. Thus  $Rmax$  is constant for all localization events.

## 2.4. Simulations for aCBC

To evaluate the performance of aCBC a series of simulated datasets of two-color localizations with known percentage of colocalization were generated. First, the centers (XY) of grouped single-molecule localizations (hereafter localization clusters) following a bidimensional Gaussian distribution with a user defined mean and sigma size values for the first emitting channel (Ch1) were generated within a constant area defined by a circle with radius =  $3\text{ }\mu\text{m}$  (i.e. emulating the cell nucleus). The center positions of an user-defined percentage of Ch1 localization clusters are also attributed to a subset of the clusters generated for the second channel (Ch2), which defines the percentage or fraction of colocalization. Thus 100% of colocalization is observed when all the localization cluster centers from Ch1 are attributed the same coordinates as centers in Ch2. The number of events per localization cluster follows an exponential random distribution with a user-defined mean value (i.e. the number of events per cluster can be modulated). The generated datasets of localizations were next processed using the aCBC software and analyzed as described in the main text (see section 5).

## 3. Sequential acquisition of two-color SMLM images

Two-color SMLM allow the precision of colocalization measurements to be increased up to 10-fold compared to diffraction-limited methods and particularly enable the measurement of distances between proteins at the single-molecule level. Thus, the outcome of experiments can be severely affected by systematic errors such as those related to the optical system (e.g. chromatic aberrations) and/or the spectral properties of the detected fluorophores (e.g. crosstalk between the different species) [33]. As for conventional microscopy, in SMLM two-color experiments the signal from the different detection channels may be recorded simultaneously or sequentially and different analysis modalities can be implemented to correct for errors in multicolor experiments [11,17,34,35].

When choosing to perform simultaneous SMLM acquisition, spectrally separated fluorophores that are simultaneously activated and individually detected by splitting the camera chip with a dichroic-based emission splitter [36,37]. To correct for chromatic aberrations in this configuration, an image registration step is required. While convenient for live-cell applications, the observation area is reduced at least twice and, in

the case of large cells, the experiment throughput is significantly reduced. Alternatively, using activator-reporter dye pairs (STORM), the same reporter dye and detection channel may be used while activating different activator dyes with lasers of different wavelengths [23]. No image registration is required here, however, the system suffers from channel crosstalk that needs to be evaluated and removed in a complex post-processing step. For fixed-cell applications where no dynamic information is sought, such as discussed in the present work, the sequential acquisition mode may be applied. Spectrally separated dyes are activated and detected at different time points of the acquisition, which overcomes several limitations of simultaneous imaging: 1- it minimizes channel crosstalk, 2- the whole field of view (FOV) can be used for each of the colors, and 3- the optical setup needs no modifications with respect to single-color acquisitions. The individual acquisition steps for sequential two-color SMLM are summarized in [Figure 1a](#). The use of separate detection channels leads to a chromatic offset in the resulting images on the camera in all three spatial directions. Chromatic aberrations in the lateral direction result in image distortions such that the same object detected in the two channels appears at different positions on the camera ([Fig. 1b upper panels](#)) that are corrected during post-processing ([see section 4.2 and Fig. 1b lower panels](#)). The focus is also shifted between the two emission channels. This is revealed as a difference between fluorescence intensity distributions along the axial direction for the same bead observed in both detection channels ([Fig. 1c](#)). This shift is systematic, relatively constant between fields of view (FOVs) and can be easily corrected by fitting a gaussian distribution to each intensity profile and computing the distance between the peaks ([Fig. 1c](#)). For the experiments described here, with emission detection centered at 700 nm (AF647) and 600 nm (mEos2) and with the imaging planes at ~3-4  $\mu\text{m}$  deep into the sample, the focus shift between channels is typically  $500 \pm 70 \text{ nm}$  ([Fig. 1c](#)).

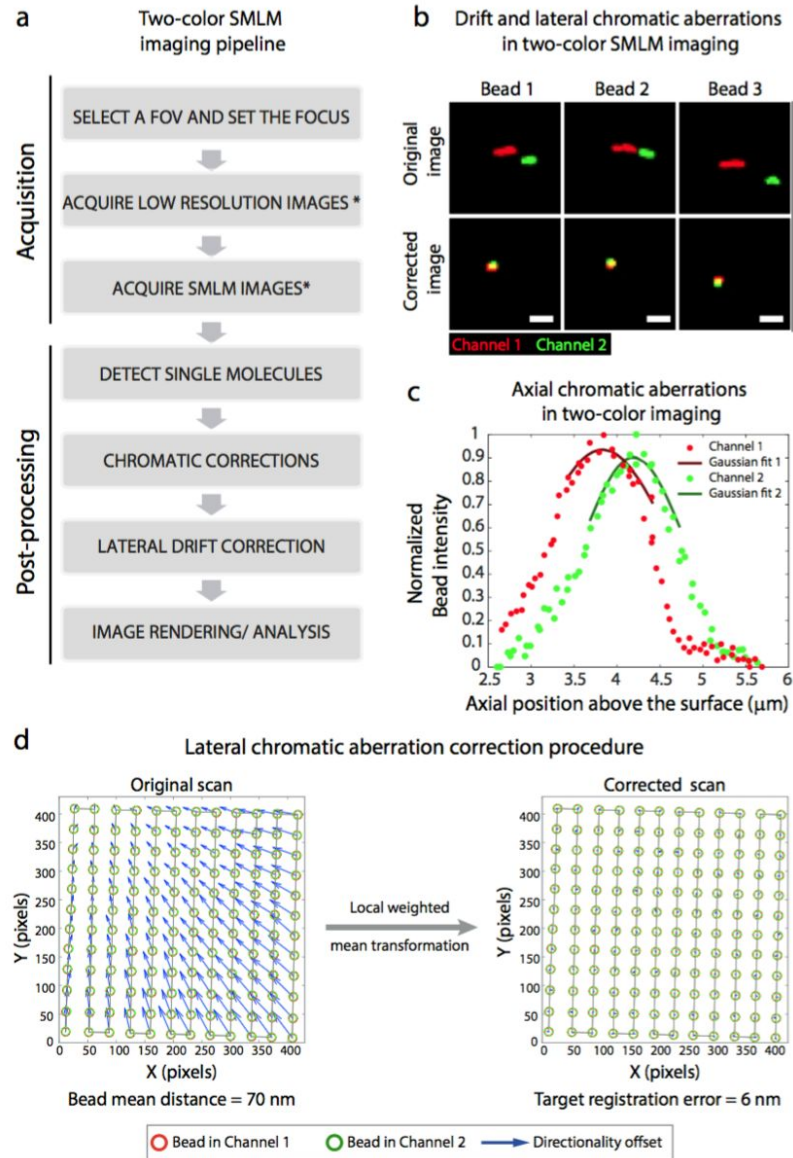


**Figure 1. Sequential two-color SMLM imaging procedure.** (a) Acquisition and post-processing pipeline in two-color SMLM. The asterisk in steps 2 and 3 indicates that the focus must be adjusted before the acquisition in the second channel. (b) Top: Reconstructed two-color SMLM images of three Tetraspeck beads from the same field of view and separated by  $>10 \mu\text{m}$  from one another, before processing. Note that the lateral drift over the acquisition of 20,000 frames per channel is reflected by the elongated trace-like images of the spherical beads. Images from the red and the green channel do not overlap due to chromatic aberrations in addition to drift. Bottom: The same beads but after drift and chromatic shift correction. Scale bar: 50 nm. (c) Focus shift in two-color acquisitions of spectrally separated fluorophores at 700 nm (Channel 1) and 600 nm (Channel 2). The normalized bead intensity in each channel was fit with a Gaussian function in a region of  $\pm 500 \text{ nm}$  around the maximal intensity. The

*peak of the curve indicates the position of the focus plane of the bead. The difference in the intensity maxima is used to adjust the focus before starting the acquisition in the second channel. (d) Bead scan for image registration. Left: raw localization plot of a single bead at each position on the field of view. Blue vectors indicate the extent and directionality of the local chromatic offset, which is inhomogeneous in the field of view. Before correction (left panel, original scan) the mean distance for the bead emitting in the red and green channels is  $D=70$  nm. After registration (right panel, corrected scan) using the “local weighted mean” transformation, bead positions are corrected and the target registration error ( $TRE=7$  nm) indicates a substantial improvement in coincidence of the XY bead coordinates (note that blue arrows are too small to be seen in this image).*

In conventional microscopy, the lower wavelength acquisition is performed first, in order to preserve the sample from photobleaching. In dSTORM experiments, no substantial difference was observed when the order of channels was switched (unpublished data). In PALM/dSTORM acquisitions though, when fluorescent proteins are detected in one of the channels, it is preferable to image first the protein channel as the continuous activation laser (405 nm) powers are lower than for organic dyes (i.e. when performing dSTORM imaging first, the higher power required for the 405 laser will photo-activate most mEos2 proteins and the PALM experiment will not yield any detectable fluorescent events). In this work we have used mEos2 and AF647 as a PALM/dSTORM pair for two-color imaging. Alternatively, spectrally separated fluorophore combinations such as AF647 with Cy3B [38], AF647 with tetramethylrhodamine (TMR) [39], and AF647 with AF750 [24], have been successfully used. Critical parameters for the choice of fluorophores in two-color SMLM are minimal overlap of excitation (STORM, using activator-reporter pairs) or emission (dSTORM, PALM) spectra, as well as compatibility in the photoswitching performance with respect to the mounting medium [40].

## **4. Data post-processing and analysis**

Following the acquisition of two-color SMLM films, the final images are obtained after several steps of processing (Fig. 1a, [post-processing](#)):

### **4.1. Single-molecule detection and localization**

Several software packages are currently available to perform single-molecule detection and localization and their number continues to increase. All of them present advantages and limitations in terms of detection performance, localization precision, analysis time and ease of user interaction (for review and comparison see [41]). In this work we employed two localization algorithms: 1- the Localization Microscopy plugin in Micromanager [42], and 2- Multiple Target Tracking (MTT) [43]. The former is very convenient for its speed and good performance and was mainly used during acquisition to check the quality of the samples

and films. The latter method is slower, however it yields superior detection efficiency and accuracy and was used for final single-molecule localization and image reconstruction.

#### **4.2. Chromatic aberrations correction**

In sequential two-color experiments, lateral distortions of the image are observed between the different colors (Fig. 1b upper panel). This error in the positioning of the same object can be corrected by an operation termed image registration. One of the images is selected as reference and the second image is geometrically transformed (for example by translation, scaling, and rotation) to match with that reference. For superresolution images, we applied a local nonlinear (local weighted mean) transformation yielding nanometer registration precision following the algorithm described in [44]. First, a fluorescent bead emitting in both channels is scanned across the field of view (FOV) and short films (~30 frames) are acquired sequentially in each detection channel at every position (Fig. 1d, left panel). Usually, for a  $45 \times 45 \mu\text{m}$  FOV, a scan of  $12 \times 12$  reference bead positions yields satisfactory results, however the denser the distribution of reference positions, the better is the correction. Next, the bead positions are detected using MTT and the spatial transformation required to align images is calculated (Fig. 1d, right panel, [44]). Finally the quality of the lateral distortion correction is evaluated. For this, the precision of registration, defined as the target registration error (TRE) is calculated as described in [45]. In our hands, TRE typically ranged between 5 and 10 nm, as reported to be the range of this method's maximum precision [32,45]. Only bead scans with  $\text{TRE} < 10 \text{ nm}$  are used to correct for chromatic aberrations. Once the spatial transformation of reference points has been calculated and validated, the transformation is applied to localizations in the sample.

#### **4.3. Lateral drift correction**

During image acquisition sample drift occurs due to thermal fluctuations, mechanical relaxation, and vibrations. This can dramatically affect the localization precision and also the final reconstructed image. To correct for lateral drift in sequential two-color acquisitions (Fig. 1b, upper panel) fluorescent beads emitting in both imaging wavelengths are used as fiducial markers. Beads are localized in each frame using the MTT software. Next, chromatic aberration correction is performed as described above and localization coordinates from the two channels are concatenated to form a single dataset. Drift correction is performed using a custom algorithm [30] and then localizations with corrected positions are reattributed to their respective detection channels for image reconstruction and colocalization analysis.

#### **4.4. Segmentation**

With the goal of analyzing individual cells, segmentation is a convenient post-processing step in which the FOV is split into regions of interest (ROIs). Ideally, each ROI contains a single cell, thus localizations from different cells on the same image can be classified and analyzed separately. In the case of SMLM, a  $45 \times 45 \mu\text{m}$  FOV contains thousands of localizations in each color (typically  $\sim 10^5$ ), which may be

challenging due to computer power limitations. After drift and chromatic aberration corrections, ROIs can be selected using either a manual selection procedure or an automatic segmentation algorithm. For the latter, low resolution epifluorescence images (DAPI stained nuclei or complexes with homogeneous distributions within the nuclear compartment) acquired before the SMLM stack can be employed.

#### **4.5 Image reconstruction**

Once the ROIs have been selected the super-resolution image of the structures of interests within each cell can be obtained. Image rendering or reconstruction is a post-processing step required to retrieve the localization information from SMLM experiments into pixel-based images. SMLM imaging yields a list of discrete spatial coordinates that are converted to pixels to form a final image. This process can be performed in several ways. One method is the representation of localization coordinates as a 2D histogram in which the intensity is proportional to the number of localizations in a given pixel with a user-defined size. Another method is a widely applied rendering approach, in which the intensity associated with each localization event is spread on the surrounding pixels with a Gaussian distribution of standard deviation equal to the experimental localization precision. The pixel size is defined by the user and is typically three to four times smaller than the localization precision ( $\sim 20$  nm).

### ***5. Quantitative analysis of colocalization in two-color SMLM imaging***

When employing diffraction-limited microscopy the most common approach to evaluate colocalization is to present results as a simple overlay composed of the different channels, each image being pseudo-colored using an appropriate color lookup table. However, it is well known that this strategy does not allow for accurate quantification and may lead to false positives depending on the degree of labeling of the structure of interest and on fluorophore properties. To obtain quantitative results, the colocalization, or the degree of spatial coincidence can be estimated using different methods that are grouped in two main families: intensity correlation coefficient-based (ICCB) analyses and object-based approaches (for extended review see [6,46]).

Intensity-based approaches calculate the correlation coefficients that measure the strength of the linear relationship between fluorescence intensity for all the pixels in the first and in the second channel. This type of colocalization analysis assumes that the labeling with both fluorochromes is proportional and that the detection of both has been carried out in a linear range. This strategy is not well suited for colocalization analysis of two-color SMLM images, since the intensity in reconstructed SMLM images typically integrates the number of detections in a given pixel. In SMLM the photophysical properties of probes, particularly the blinking dynamics of organic dyes in dSTORM experiments, are key determinants of the final results. This blinking behavior depends strongly on the probe chemistry and the local environment,

and the number of detections in the second channel may not respond linearly with respect to the reference channel.

Object-based methods rely on the nature of the colocalization event and on the size, form and intensity distribution of the fluorescent signal (i.e. it relies on the structural properties of the signal). In conventional fluorescence images, segmentation into objects is performed by applying an intensity threshold on the image, whereas in SMLM is performed by grouping the individual events that are found closer than a given distance. Once the objects have been determined, their size, position and shape can be measured and structures with centers found at a distance smaller than the size of the objects (because of overlap) or smaller than the resolution of the technique (~20 nm in SMLM) can be thus considered colocalized. The main drawback of this approach arises when studying protein assemblies of complex structural features (i.e. the geometry or shape may bias the determination of the object center) and additionally, using this strategy, the gain in information concerning individual molecules is lost when regrouping them into a large object that may, eventually, include several protein complexes.

### 5.1. Single-molecule colocalization quantification strategy

To overcome the above mentioned limitations of traditional colocalization methods, a recently developed approach for single-molecule colocalization quantification was implemented (Coordinate-Based Colocalization analysis (CBC), [see section 2.3](#), [32]). The main advantage of this procedure, when applied to SMLM imaging compared to ICCB and object-based approaches, is that detection coordinates can be used for colocalization analysis without the need of additional image processing steps, avoiding the main source of errors of colocalization analysis when using thresholding or when grouping single-molecule detections into objects. The procedure is, in principle, analogous to the ICCB strategy [47], but in CBC a colocalization coefficient ( $C_A$ ) is attributed to each single-molecule localization in each detection channel ([see section 2.3](#), [32]).  $C_A$  can adapt values comprised between -1 for negative correlation (interpreted here as spatial proximity but lack of overlap between the two signals) and 1 for complete positive correlation (colocalization), while weak correlation coefficients (typically 0-0.3) indicate no colocalization.

Since  $C_A$  is calculated for all detection events, this type of analysis may require prolonged time for computation. For example in our experiments a *Drosophila* nucleus with 50,000 events per channel is analysed in ~100 sec using a computer with a 2.8 GHz processor and 14 GB of RAM. Consequently automation of the CBC calculation is to be considered. In this work, we implemented the CBC method within an algorithm allowing to perform automated whole-cell analysis (aCBC). The determination of the optimal parameter values used to analyze colocalization experiments requires special attention ([see next section](#)). The calculation of  $C_A$  requires three types of input: the localization coordinates from the two detection channels, the distance interval to be explored around each single-molecule in both channels ( $r$ ), and the size of the region to analyze ( $R_{\max}$ ). The values of the last two ( $r$  and  $R_{\max}$ ) are user defined and are key to



accurately evaluate single-molecule colocalization since: 1) for each detection event, all the localizations found outside the area defined by  $R_{\max}$  are considered uncorrelated and 2)  $r$  defines the resolution of the aCBC analysis (notice that the number of bins of each distance distribution histograms ( $D_{A,B}$ ,  $A$  and  $D_{A,B}$ ) calculated from Eq. 1 and 2 is defined by the  $R_{\max}/r$  ratio, [see section 2.3](#)). Therefore, several repeats of the analysis should be performed by varying the values of this parameters to find the optimal values ([see next section](#)) while considering the size of the structures under study, the distance between them in the two-color image and the SMLM resolution.

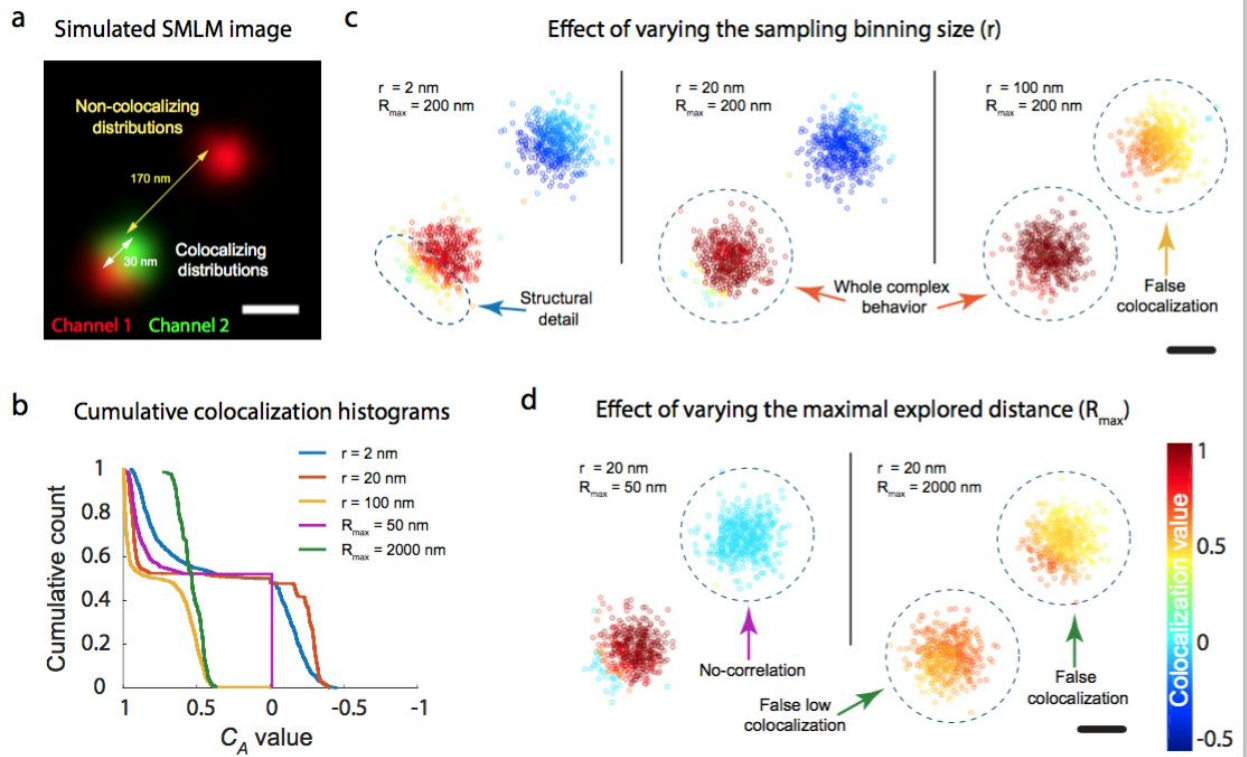


**Figure 2. Evaluation of aCBC colocalization analysis parameters**

**(a)** Composite reconstructed image of 3 clusters of SMLM localizations (two in channel 1 - red, and one in channel 2 - green, see main text). The SMLM Gaussian distributions contain 500 localizations each, and have the same size ( $\sigma = 30$  nm). **(b)** Cumulative single molecule histograms of  $C_A$  values for the different simulations displayed in panel C.  $r$  and  $R_{\max}$  were systematically varied while keeping the other parameter constant ( $r$  and  $R_{\max}$  values are indicated on the inset, constant  $R_{\max} = 200$  nm and constant  $r = 20$  nm) **(c-d)** Single molecule colocalization coefficient maps for simulated data from panel a for **(c)** constant  $R_{\max}$  and **(d)**  $r$ , while varying  $r$  and  $R_{\max}$  respectively. Arrows indicate different colocalization outputs depending on parameter values and highlight structural details (see main text) and are color-coded according to the colormap in panel d. The color scale in panel d (Colocalization values,  $C_A$ )

*reflects the degree of colocalization between single molecules from blue (anticorrelated) to light blue (no correlation) and red (complete correlation). Scale bars: 100 nm.*

## 5.2. Evaluation and optimization of aCBC for colocalization quantification

Depending on the experiment and the sample, one may wish to probe very locally for colocalization and exclude from analysis structures that are considered out of range for a given cellular component. Also the size, shape and distribution of the studied markers, as well as the spatial resolution of the image are to be considered for the determination of aCBC parameter values. To evaluate the impact of the two key input parameter values ( $r$  and  $R_{\max}$ ) on the output of the aCBC analysis, a simple case was considered. A synthetic two-color reconstructed image was generated (Fig. 2a), in which the first channel (red) represents two Gaussian distributions of single-molecule localizations, found at a peak to peak distance of 200 nm from one another (red clusters in Fig. 2a). In the second channel (green), a subset of single-molecule events, also following a single Gaussian distribution, is partially colocalizing (lower green cluster in Fig. 2a) with one of the red clusters, with a peak to peak distance of 30 nm. The peak to peak distance between the centers of the non-colocalizing green and red distributions of single-molecule events is 170 nm. All the distributions contain 500 localizations and have the same size ( $\sigma = 30$  nm).

The cumulative histograms of colocalization values (Fig. 2b) and the respective colocalization maps (Fig. 2c-d) of localization events from the red channel illustrate the differences in output that can be obtained for the same situation by varying either  $r$  or  $R_{\max}$ , while keeping the other parameter constant. For a constant value of  $R_{\max}$ , when  $r$  is small (2 nm), the analysis finely probes the distances between localizations and results in smoothly distributed positive correlation values for the lower distributions, and negative correlation values for the upper distribution (Fig. 2b blue curve and Fig. 2c left panel). Note that in the colocalizing distributions, when using this binning value for  $r$  additional structural features of the colocalizing molecules can be resolved, as the events in the red channel that strongly overlap with events in the green channel can be differentiated from the events that are in close proximity but overlap with only a small number of events from the green channel (arrow in Fig. 2c left panel). When  $r$  is increased to 20 nm (Fig. 2b orange curve and Fig. 2b, middle panel), the events from the colocalizing distributions in the lower cluster show a higher homogeneity, clearly indicating colocalization between the distributions but sacrificing part of the single-molecule structural details that could be recovered for smaller  $r$  values. When  $r = 100$  nm (Fig. 2b yellow curve and Fig. 2c right panel), a single bin of the distance histograms comprises the large majority of the events from each cluster. The events from the colocalizing structure display similar values to the previous conditions, although non structural details are observed. However, the events from the non-colocalizing cluster are considered as positively correlated, and a wrong conclusion of colocalization may be drawn (Fig. 2c right panel). As stated above,  $R_{\max}$  determines the distance up to which the correlation between localization events is probed. For  $R_{\max}$  values smaller than the size of the distributions ( $R_{\max} = 50$  nm, Fig. 2b magenta curve and Fig. 2d left panel), the colocalizing distributions display high

colocalization values, whereas all the events from the non-colocalizing distributions display no correlation (magenta arrow in Fig. 2d left panel and note magenta solid line dropping sharply at colocalization value = 0 in Fig. 2b). At  $R_{\max} = 2000$  nm, which is one order of magnitude larger than the maximal distance between the furthest green and red distributions (170 nm, peak to peak), all the population information is lost and both red distributions partially colocalize with the green distribution (Fig. 2b green curve and Fig. 2D right panel). This is due to the fact that  $R_{\max}$  and the number of events contained in that radius (see Eq. 1 and 2 in section 2.3) act as a normalizing factor, that in this case will have a deleterious effect over the correlation between single-molecules probed at small distances.

Therefore, before evaluating colocalization using the aCBC approach, a careful visual inspection of the obtained images and evaluation of the sizes and density of the complexes under study, as well as the image reconstruction parameters (localization precision, pixel size) should be considered. The optimal value of  $r$  and  $R_{\max}$  is a tradeoff between the degree of structural detail that can be revealed for colocalizing single-molecules and the minimal threshold that will define non-colocalizing events. Values of  $r$  should not overestimate the experimental single-molecule localization precision (including chromatic aberration and drift corrections) or average out structural details of the complexes under study (20-30 nm in our experience). On the other hand,  $R_{\max}$  values should be adapted to include the full size of the single-molecule distributions associated to one complex (ideally  $R_{\max}$  should be set to  $\sim 10$  times the standard deviation of the single-molecule localization distributions) and should be lower than the minimal average distance separating non-colocalizing distributions. Clearly,  $r$  is more influenced by the quality of the images obtained while  $R_{\max}$  is more dependent on the structural characteristics (e.g. size and spatial distribution) of the structures under study. Thus, knowledge on the structure of interest, prior to aCBC analysis may be helpful to determine the input parameters.

### 5.3. Evaluation of aCBC performance

The aCBC analysis provides a method to determine the extent of colocalization with a detail potentially down to the single-molecule resolution. In the previous section we evaluated the response of the algorithm to the input parameter values. In this section, to further test the performance of aCBC in complex samples and establish a robust colocalization quantification procedure, SMLM datasets with known colocalization levels were generated and analyzed.

First, a complete and partially colocalizing dataset were simulated and the resulting 2-color reconstructed image is shown in Fig. 3A. The dataset consists of a random distribution of localization clusters (100 in Ch1 and 200 in Ch2) with a size of  $20 \pm 5$  nm, and a mean of 50 events per cluster. In the first channel (Ch1), the centers of all clusters completely overlap with centers of clusters in the second channel (Ch2). This dataset was analyzed with aCBC and the colocalization coefficient ( $C_A$ ) maps of the individual localizations are shown in Figure 3b. As expected, the vast majority of localization events in Ch1 display high correlation coefficients, and from the cumulative histogram (Fig. 3c) it appears that 93% of

$C_A > 0.5$ . In contrast, in Ch2, where only half of the clusters colocalize with clusters from Ch1, three distinct populations of events can be distinguished (Fig. 3c). The largest population is composed of positively correlated distributions (~60%). A second population is defined by non-correlated distributions with  $C_A = 0$  (~30% of events). The third population contains negatively correlated events (~10 %), which correspond to localization events that are positioned in proximity, but do not overlap with localizations from Ch1. This analysis confirms that aCBC can accurately detect 100% colocalizing events and also discriminate different population behaviors when events partially colocalize.

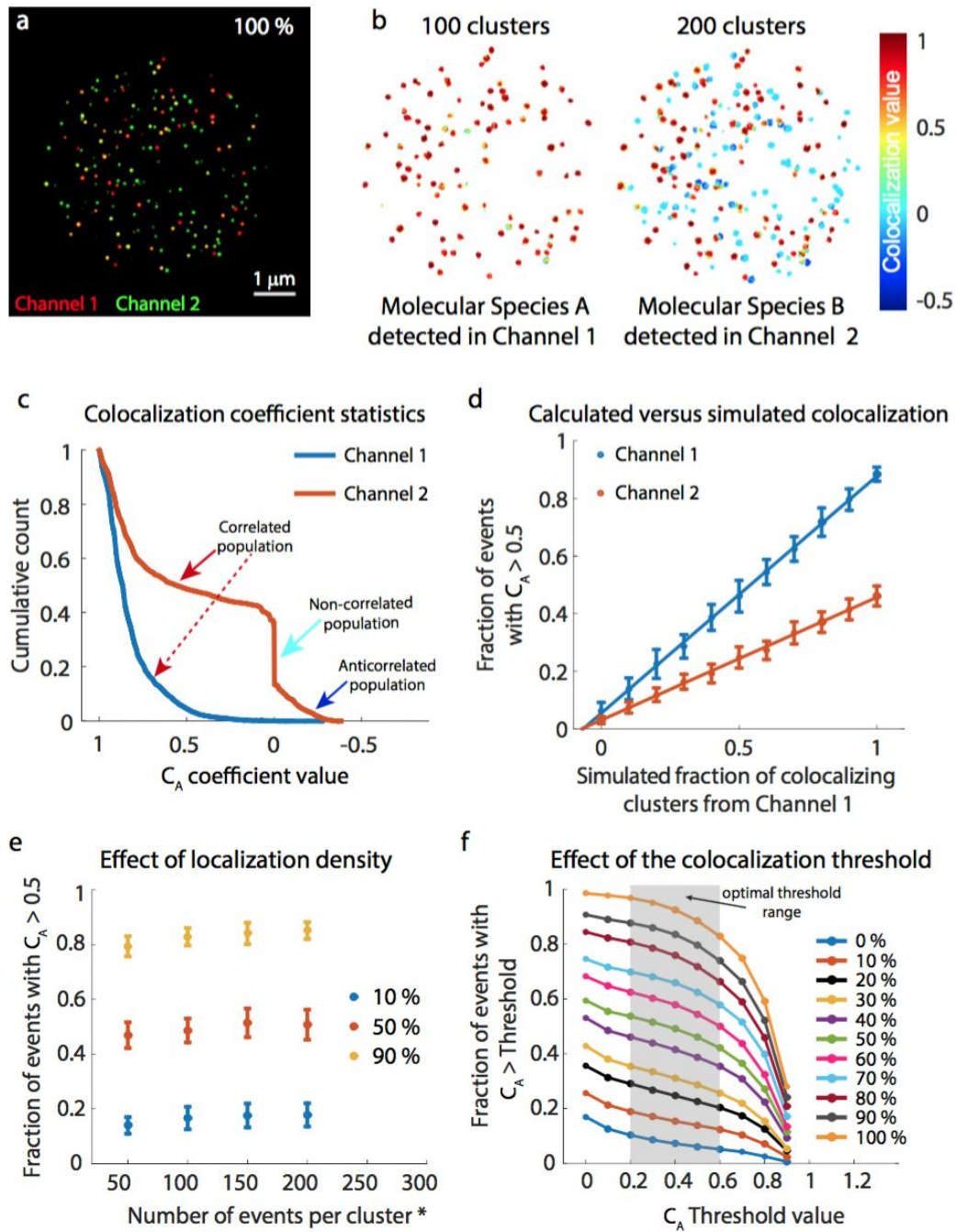


**Figure 3. Evaluation of aCBC performance for complex samples**

(a) Composite reconstructed image of a simulated two-color SLM dataset with 100% colocalization between events detected in Channels 1 and 2 (see main text). Scale bar: 1  $\mu\text{m}$ . (b)  $C_A$  coefficient maps of localizations after aCBC analysis for the dataset in (a) color-coded according to the colormap on the right. (c) Cumulative colocalization values ( $C_A$ ) histogram for the single-molecule events from analysis in panel (b). Blue and orange solid lines correspond to  $C_A$  values of localizations in Channel 1 and Channel 2

respectively. Arrows indicate the different populations revealed by the aCBC analysis with the color-code of colocalization values of panel **b** (see main text) **(d)** Effect of varying the degree of colocalization on the aCBC output. The  $C_A$  coefficients were calculated for Channel 1 (blue) and Channel 2 (orange) when varying the degree of simulated colocalization. Each data point is the mean percentage of events with  $C_A > 0.5$  (obtained from cumulative histograms equivalents to those depicted in panel **c** from 30 simulations at each level of colocalization. The error bars indicate the standard deviation of the mean values. Solid blue and dotted orange lines are linear fits with  $R^2$  of 0.999 and 0.998 respectively highlighting the simple linear relationship between true colocalization and aCBC output. **(e)** Effect of the mean number of events per cluster for 3 levels of colocalization (10%, 50% and 90%) on the colocalization analysis. The  $C_A$  coefficients were calculated when varying the degree of simulated colocalization and the mean number of events per localization cluster. Each data point is the mean fraction of events with  $C_A > 0.5$  for events in Channel 1 from 30 simulations. Error bars indicate the standard deviation of the mean values. **(f)** Effect of the threshold on the resolution of the aCBC method. aCBC analysis was performed for colocalization situations from 0 to 100% (see color code on the right) and the fraction of events with  $C_A > \text{threshold}$  were calculated for Channel 1 as explained in the main text. Data points and error bars are as in **e**. The optimal threshold range is highlighted with the grey area.

Next, to evaluate the response of aCBC to the total number of colocalizing clusters, the percentage of colocalization between the two channels was varied between 0 and 100%. The colocalization values for 30 independent simulations were calculated and the fraction of events with  $C_A > 0.5$  was computed (Fig. 3d). A strong linear dependence is observed between the fraction of simulated colocalizing events (X axis) and the fraction of events with high colocalization coefficients (Y axis), confirming the high sensitivity of aCBC to variations in the degree of colocalization and its ability to detect colocalization fractions of events as low as 10%. To further test the robustness of the method with respect to the density of detected events, we varied the mean number of events per localization cluster and calculated the fraction of events with  $C_A > 0.5$  for three levels of colocalization (Fig. 3e). In all cases, the simulated and calculated fraction of colocalizing events showed very good agreement. These results have a significant implication in the colocalization analysis of SMLM experiments. In particular, two SMLM acquisitions of the same markers may yield a variable number of localizations between different acquisitions. The robustness of the aCBC method allows the combination of datasets, which differ in the density of events per cluster, without affecting the results of the colocalization analysis.

Finally, to determine the optimal  $C_A$  value threshold, the dataset from Figure 3d was analyzed with a series of thresholds ranging from 0 to 0.9 (Figure 3F). As expected, the increase of the threshold value leads to a decrease in the fraction of events with aCBC coefficients above the threshold. The evolution of these values is monotonous and symmetrical for the different percentages of localization clusters overlap up to a



threshold value of 0.6. For thresholds above 0.6 the data points start to converge, thus decreasing the capacity to discriminate between the different colocalization conditions. The impact of the threshold value is the smallest in the range 0.2-0.6 with very similar resolution, indicated by the distance between points along the Y axis for a given threshold value. Therefore, it can be concluded that the analysis with an aCBC threshold of 0.5, which indicates high level of spatial correlation, can efficiently discriminate between different colocalization conditions. Note that for simulated colocalization percentages below 50% the use of  $C_A$  threshold below 0.4 can lead to an overestimation of the relative number of positively correlating events. This is particularly significant for the cases where the simulated fractions of colocalizing events are below 0.3. Also a further analysis of the curve of non-colocalizing events (0% in Fig. 3d) shows that the aCBC method can account for ~20% of false positive localizations for very low  $C_A$  thresholds that drop to less than 5% for  $C_A$  thresholds above 0.5.

Taken together, these results demonstrate that the aCBC implementation for single-molecule colocalization analysis is a robust and simple to interpret method that can be applied on complex datasets such as the clustered localizations distribution of nuclear factors imaged by two-color SMLM. The performance of the analysis is tightly dependent on the imaging resolution, which in turn is affected by the sample preparation conditions, as well as by the image acquisition and post-processing. It is then crucial to validate the good quality of these experimental steps, prior to performing analyses to reach biologically-significant conclusions.

## 6. Two-color SMLM imaging and colocalization analysis of nuclear factors

In the present section, a simple procedure for the quality control of SMLM images is introduced. Through the example of the *Drosophila* nuclear protein Beaf-32, displaying a homogeneous distribution in conventional microscopy (Fig. 4a), we propose a workflow for the assessment of the labeling efficiency and specificity at the enhanced structural detail provided by super-resolution imaging, by means of the aCBC analysis.

The increased resolution of SMLM methods introduces additional experimental factors, which must be tightly controlled to obtain images with optimal quality and biologically relevant results. A critical parameter in the context of fluorescent labeling for super-resolution microscopy is the fluorescent tag size, especially in the case of fluorescent immunostaining (IF). A classical configuration of affinity labeling of biological samples is the use of a primary antibody targeting the structure of interest, and a secondary antibody bearing the fluorophore molecule (also known as indirect immunofluorescence). Although it is widely accepted that the tag size in SMLM imaging influences the experimental spatial resolution, protocols that use indirect labeling still prevail, although this labeling method is applicable in SMLM only if it is demonstrated that the tag size does not affect the final image. Here, we describe an experimental procedure

allowing fluorescent labeling performance to be evaluated in a single step for both transfection and IF through the quantitative colocalization analysis of a doubly labeled protein (Beaf-32). This strategy also demonstrates the detrimental effect in colocalization precision by the use of fluorescently labeled high molecular weight affinity probes.

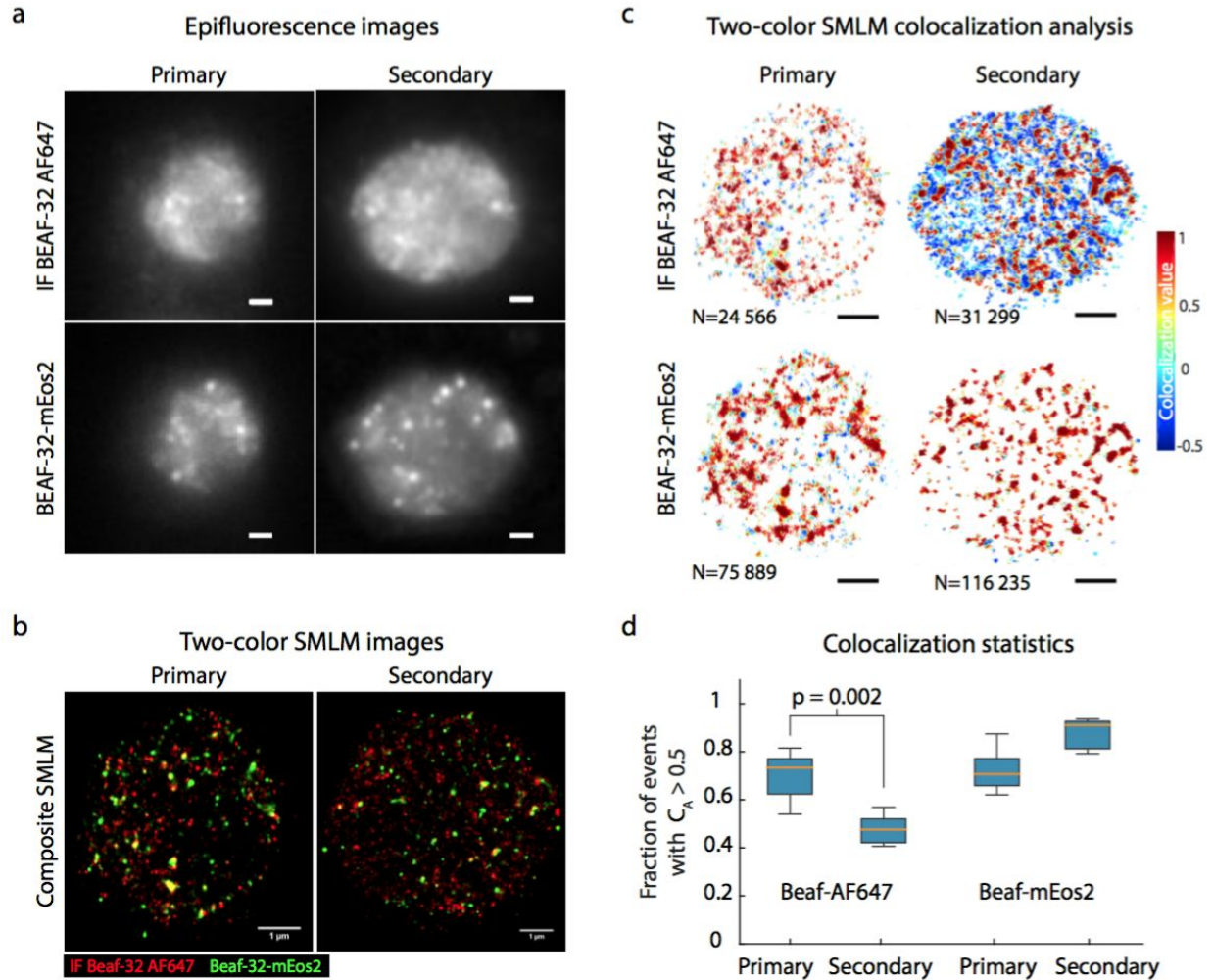


**Figure 4. Effect of the fluorescent tag size in SMLM experiments revealed by aCBC**

**(a)** Conventional fluorescence images of representative *Drosophila* S2 cells immunostained with either a primary fluorescently-labeled (upper left) or a secondary fluorescently-labeled antibody (upper right) and previously transfected with (lower panels) Beaf-32-mEos2. **(b)** Composite reconstructed SMLM images of the cells depicted in panel **a**. Reconstruction parameters: pixel size = 8 nm, width of the Gaussian for reconstruction = 15 nm. **(c)**  $C_A$  coefficient maps of localizations after aCBC analysis for localization in the AF647 (top panels) and mEos2 channels (bottom panels) for cells labeled with primary only (left panels) and with secondary antibodies (right panels). The numbers (N) at the bottom of each cell correspond to the number of single detections in each map obtained in 20,000 frames and are an indication for the



density of events. The color scale on the right (Colocalization values) reflects the colocalization coefficient of single localizations. **(d)** Statistics of the colocalization for the Beaf-AF647 (left) and Beaf-mEos2 (right) channels for experiments of direct IF (Primary, N=14) or indirect IF (Secondary, N=11). Boxplots indicate the median (orange bar), 25th and 75th percentile limits (blue areas), and extreme values (whiskers) of the fraction of events with  $C_A > 0.5$ . The p-value ( $p=0.002$ ) indicates significantly higher colocalization for events in the AF647 channel detected in the direct IF condition (Primary), obtained from a one-way Kolmogorov-Smirnov test. Scale bars in all panels: 1  $\mu\text{m}$ .

### 6.1. Dual color protein staining as an image validation strategy

To evaluate specificity at high spatial resolution, a simple control is to perform a two-color imaging experiment by labeling the same factor with two spectrally different fluorescent tags. For this, the *Drosophila* protein Beaf-32 was immunostained with either a primary antibody coupled to AF647 (direct IF; Fig. 4a, upper left panel) or by indirect IF (Fig. 4a, upper right panel). The same cells were transiently transfected with a Beaf-32-mEos2 fusion (Fig. 4a lower panels). The low resolution images of the representative cells depicted in Fig. 4a for both transfection and IF demonstrate that the Beaf-32 signal is specifically localized within the nucleus and the fluorescence is homogeneously distributed. Some local protein enrichments can be observed in the Beaf-32-mEos2 images. The correspondence between the signal distributions of the IF and transfection experiments is an indicator of efficient labeling both in IF and transfection and is a useful preliminary control. At this stage, the direct and indirect IF protocols seem to yield similar results.

### 6.2. Tag size effect on the colocalization analysis accuracy

Beaf-32-bound antibodies coupled to AF647 should be found in tight spatial proximity to Beaf-32-mEos2. Therefore, a strong spatial correlation is expected between the two markers. A visual inspection of composite rendered SMLM images (Fig. 4b) reveals similar patterns of localizations between the primary and secondary antibody conditions. However, in superimposed two-color images the colocalization is underestimated due to differences in intensities between the two channels. Indeed, the characteristic yellow color indicating colocalization is only perceived in very high intensity pixels.

To better assess colocalization, quantitative analysis was performed using aCBC (Fig. 4c). The aCBC analysis of the primary antibody staining experiment shows a very good concordance of single-molecule colocalization (Fig. 4c, left upper panel). Similar quantification values are observed when evaluating colocalization of BEAF-32-mEos2 against AF647 (Fig. 4c, left lower panel). When evaluating colocalization of BEAF-32 labeled with secondary-AF647 antibody against mEos2 (Fig. 4c right upper panel), a large population of AF647 localizations depicts negative correlation coefficients (~39%, Fig. 4c right upper panel), whereas colocalization of BEAF-32-mEos2 against secondary-AF647 still shows high level of positive correlation.

Next we quantified the fraction of events with  $C_A > 0.5$  in a larger number of cells after direct (N=14) and indirect (N=11) fluorescent immunostaining. BEAF-32 labelled with primary antibody and mEos2 showed high colocalization when observed in both channels (Fig. 4d) indicating that the BEAF-32-mEos2 protein is efficiently bound by the primary antibody and that the pool of non-labelled endogenous BEAF-32 is very low (i.e. absence of anticorrelated and non-correlated events in both channels). For secondary antibody labelling, strong correlation is still observed for BEAF-32-mEos2 (Fig. 4d) whereas secondary-AF647 localizations show lower levels of colocalization, particularly due to a high level of anticorrelation (blue-cyan events on Fig. 4c right upper panel). This results indicates close spatial proximity but no overlapping of events between channels, suggesting that the distance between mEos2 and AF647 molecules is increased due to the presence of the secondary antibody in addition to the primary. Indeed, the negatively correlated population is strongly reduced in direct IF (compare blue-cyan dots in Fig. 4c upper panels). It is known that the use of secondary antibodies increases the effective size of the probe and therefore the distance range between the fluorophore and the target molecule, thus deteriorating the spatial resolution. Considering the size reported from crystallographic structures (e.g. 1IGT) and the labeling accessible sites, fluorescent dyes coupled directly to the primary antibody are found at < 8-15 nm from its target, which falls within the localization precision of SMLM instruments, whereas the addition of a secondary antibody increases that distance limit up to two fold. It could be expected then, that further reducing the affinity probe size, such as by using only the antigen binding fragment of primary antibodies or smaller tags (e.g. nanobodies targeting the endogenous protein of interest [37]) would further increase the accuracy and resolution of cellular structures using two-color SMLM.

## 7. Concluding remarks

Several technical limitations thwart the widespread use of multi-color single-molecule localization microscopy to investigate the assembly mechanisms and regulation of complex cellular structures and machineries. This article provides technical guidance to perform multi-color SMLM imaging and analysis of interacting nuclear complexes in eukaryotic cells. We focus on key aspects of sample preparation, imaging conditions, postprocessing and single-molecule colocalization analysis.

Successful SMLM relies strongly on the quality of the sample. Immunolabeling of intracellular components requires fixation and permeabilization, which can severely affect the integrity of the imaged structures. As ultrastructural perturbation induced by these sample preparation steps may be epitope-specific and observation of biological specimens at the spatial resolution provided by SMLM is a fairly recent research area, it reveals challenging to establish universal protocols. It remains central that validation of immunolabeling experiments is systematically performed by comparison with live-cell imaging [48], fixation buffer optimization [49], and correlative approaches [50]. Special attention should be paid to

imaging samples several days after fixation. In our hands samples did not yield satisfactory results when imaged more than 1-2 days after preparation. The immunofluorescence protocol presented here uses 2-5 times higher concentration of primary antibodies compared to protocols for confocal microscopy. Indeed, the increase of antibody concentration led to a significant improvement of labeling densities. However, increasing the antibody concentrations may lead to nonspecific binding and an optimization step is required to discard staining specificity issues. The double labeling quality control strategy presented in the final section of this article is well adapted to evaluate specificity of fluorescent staining with primary antibodies at sub-diffraction resolution. A crucial parameter in dSTORM is the photoswitching environment, which includes the efficiency of oxygen depletion, the stability in pH, and illumination power densities. It is then expected that the photoswitching properties of organic dyes vary from one experimental setup to another. Imaging conditions (laser powers, temperature regulation, sample mounting) are other factors that may vary between laboratories and affect dye performance.

We introduce and experimentally validate automated Coordinate-based Colocalization analysis (aCBC), which allows to probe colocalization between two molecular species imaged by SMLM directly at the single localization event level. The accuracy and resolution of aCBC is strongly dependent on the spatial resolution and importantly, on the registration precision between the two acquisition channels. It is of crucial importance then to only analyse datasets with superior localization precision, drift and chromatic aberration correction values. Finally, we experimentally demonstrate the deleterious effect of indirect immunofluorescence on colocalization output. Note that here we considered a situation in which one of the fluorescent labels is a fusion protein with a significantly lower molecular size than antibodies. Therefore, a larger effect of tag size on the colocalization output is to be expected in double immunolabeling experiments. Overall, the experimental and analytical parameters of multicolor SMLM discussed here are to be considered by users willing to make use of these techniques to answer biological questions.

## **Acknowledgments**

We thank Andres Cardozo Gizzi for critical reading and helpful comments. This research was supported by funding from the European Research Council under the 7th Framework Program (FP7/2010-2015, ERC grant agreement 260787). We acknowledge France-BioImaging infrastructure supported by the French National Research Agency (ANR-10-INBS-04, «Investments for the future»).

## References

- [1] T. Siggers, R. Gordân, Protein–DNA binding: complexities and multi-protein codes, *Nucleic Acids Res.* (2013). doi:10.1093/nar/gkt1112.
- [2] C.-H. Leung, D.S.-H. Chan, H.-Z. He, Z. Cheng, H. Yang, D.-L. Ma, Luminescent detection of DNA-binding proteins, *Nucleic Acids Res.* 40 (2012) 941–955.
- [3] M.C. Williams, J.L. Maher, *Biophysics of DNA-Protein Interactions: From Single Molecules to Biological Systems*, Springer New York, 2010.
- [4] T. Moss, *DNA-Protein Interactions: Principles and Protocols*, Humana Press, 2001.
- [5] E.A. Jares-Erijman, T.M. Jovin, Imaging molecular interactions in living cells by FRET microscopy, *Curr. Opin. Chem. Biol.* 10 (2006) 409–416.
- [6] S. Bolte, F.P. Cordelières, A guided tour into subcellular colocalization analysis in light microscopy, *J. Microsc.* 224 (2006) 213–232.
- [7] L. Schermelleh, R. Heintzmann, H. Leonhardt, A guide to super-resolution fluorescence microscopy, *J. Cell Biol.* 190 (2010) 165–175.
- [8] S. Cox, Super-resolution imaging in live cells, *Dev. Biol.* 401 (2015) 175–181.
- [9] M. Georgieva, M. Nollmann, Superresolution microscopy for bioimaging at the nanoscale: from concepts to applications in the nucleus, *RRB.* (2015) 157.
- [10] M. Heilemann, S. van de Linde, M. Schüttpelz, R. Kasper, B. Seefeldt, A. Mukherjee, et al., Subdiffraction-resolution fluorescence imaging with conventional fluorescent probes, *Angew. Chem. Int. Ed Engl.* 47 (2008) 6172–6176.
- [11] M. Heilemann, S. van de Linde, A. Mukherjee, M. Sauer, Super-Resolution Imaging with Small Organic Fluorophores, *Angew. Chem. Int. Ed.* 48 (2009) 6903–6908.
- [12] M.J. Rust, M. Bates, X. Zhuang, Sub-diffraction-limit imaging by stochastic optical reconstruction microscopy (STORM), *Nat. Methods.* 3 (2006) 793–795.
- [13] S.T. Hess, T.P.K. Girirajan, M.D. Mason, Ultra-high resolution imaging by fluorescence photoactivation localization microscopy, *Biophys. J.* 91 (2006) 4258–4272.
- [14] E. Betzig, G.H. Patterson, R. Sougrat, O.W. Lindwasser, S. Olenych, J.S. Bonifacino, et al., Imaging intracellular fluorescent proteins at nanometer resolution, *Science.* 313 (2006) 1642–1645.
- [15] M. Fernández-Suárez, A.Y. Ting, Fluorescent probes for super-resolution imaging in living cells, *Nat. Rev. Mol. Cell Biol.* (2008).
- [16] C.G. Galbraith, J.A. Galbraith, Super-resolution microscopy at a glance, *J. Cell Sci.* 124 (2011) 1607–1611.
- [17] H. Shroff, C.G. Galbraith, J.A. Galbraith, H. White, J. Gillette, S. Olenych, et al., Dual-color

- superresolution imaging of genetically expressed probes within individual adhesion complexes, *Proc. Natl. Acad. Sci. U. S. A.* 104 (2007) 20308–20313.
- [18] F.V. Subach, G.H. Patterson, S. Manley, J.M. Gillette, J. Lippincott-Schwartz, V.V. Verkhusha, Photoactivatable mCherry for high-resolution two-color fluorescence microscopy, *Nat. Methods.* 6 (2009) 153–159.
- [19] F.V. Subach, G.H. Patterson, M. Renz, J. Lippincott-Schwartz, V.V. Verkhusha, Bright monomeric photoactivatable red fluorescent protein for two-color super-resolution sptPALM of live cells, *J. Am. Chem. Soc.* 132 (2010) 6481–6491.
- [20] A.B. Rosenbloom, S.-H. Lee, M. To, A. Lee, J.Y. Shin, C. Bustamante, Optimized two-color super resolution imaging of Drp1 during mitochondrial fission with a slow-switching Dronpa variant, *Proc. Natl. Acad. Sci. U. S. A.* 111 (2014) 13093–13098.
- [21] J. Tam, G.A. Cordier, J.S. Borbely, A. Sandoval Álvarez, M. Lakadamyali, Cross-talk-free multi-color STORM imaging using a single fluorophore, *PLoS One.* 9 (2014) e101772.
- [22] C.C. Valley, S. Liu, D.S. Lidke, K.A. Lidke, Sequential superresolution imaging of multiple targets using a single fluorophore, *PLoS One.* 10 (2015) e0123941.
- [23] M. Bates, B. Huang, G.T. Dempsey, X. Zhuang, Multicolor Super-Resolution Imaging with Photo-Switchable Fluorescent Probes, *Science.* 317 (2007) 1749–1753.
- [24] M. Bates, G.T. Dempsey, K.H. Chen, X. Zhuang, Multicolor super-resolution fluorescence imaging via multi-parameter fluorophore detection, *Chemphyschem.* 13 (2012) 99–107.
- [25] A. Lampe, V. Haucke, S.J. Sigrist, M. Heilemann, J. Schmoranz, Multi-colour direct STORM with red emitting carbocyanines, *Biol. Cell.* 104 (2012) 229–237.
- [26] R.U. & U.S. Mohamed Kodiha, Optimized immunofluorescence staining protocol to detect the nucleoporin Nup98 in different subcellular compartments : Protocol Exchange, Stochaj Lab (McGill University), 2009. doi:10.1038/nprot.2009.16.
- [27] D.E. Mosedale, J.C. Metcalfe, D.J. Grainger, Optimization of immunofluorescence methods by quantitative image analysis, *J. Histochem. Cytochem.* 44 (1996) 1043–1050.
- [28] R.W. Burry, Specificity controls for immunocytochemical methods, *J. Histochem. Cytochem.* 48 (2000) 163–166.
- [29] R.W. Burry, Controls for immunocytochemistry: an update, *J. Histochem. Cytochem.* 59 (2011) 6–12.
- [30] J.-B. Fiche, D.I. Cattoni, N. Diekmann, J.M. Langerak, C. Clerte, C.A. Royer, et al., Recruitment, assembly, and molecular architecture of the SpoIIIE DNA pump revealed by superresolution microscopy, *PLoS Biol.* 11 (2013) e1001557.
- [31] D.I. Cattoni, J.B. Fiche, M. Nöllmann, Single-molecule super-resolution imaging in bacteria, *Curr. Opin. Microbiol.* 15 (2012) 758–763.
- [32] S. Malkusch, U. Endesfelder, J. Mondry, M. Gelléri, P.J. Verveer, M. Heilemann, Coordinate-based colocalization analysis of single-molecule localization microscopy data,

Histochem. Cell Biol. 137 (2012) 1–10.

- [33] M. Scarselli, P. Annibale, A. Radenovic, Cell Type-specific  $\beta$ 2-Adrenergic Receptor Clusters Identified Using Photoactivated Localization Microscopy Are Not Lipid Raft Related, but Depend on Actin Cytoskeleton Integrity, *J. Biol. Chem.* 287 (2012) 16768–16780.
- [34] A. Lampe, G. Tadeus, J. Schmoranzner, Spectral demixing avoids registration errors and reduces noise in multicolor localization-based super-resolution microscopy, *Methods Appl. Fluoresc.* 3 (2015) 034006.
- [35] I. Testa, C.A. Wurm, R. Medda, E. Rothermel, C. von Middendorf, J. Fölling, et al., Multicolor fluorescence nanoscopy in fixed and living cells by exciting conventional fluorophores with a single wavelength, *Biophys. J.* 99 (2010) 2686–2694.
- [36] D.J. Crossman, Y. Hou, I. Jayasinghe, D. Baddeley, C. Soeller, Combining confocal and single molecule localisation microscopy: A correlative approach to multi-scale tissue imaging, *Methods*. (n.d.). doi:10.1016/j.ymeth.2015.03.011.
- [37] J. Ries, C. Kaplan, E. Platonova, H. Eghlidi, H. Ewers, A simple, versatile method for GFP-based super-resolution microscopy via nanobodies, *Nat. Methods.* 9 (2012) 582–584.
- [38] K. Xu, G. Zhong, X. Zhuang, Actin, Spectrin, and Associated Proteins Form a Periodic Cytoskeletal Structure in Axons, *Science.* 339 (2013) 452–456.
- [39] Z.W. Zhao, R. Roy, J.C.M. Gebhardt, D.M. Suter, A.R. Chapman, X.S. Xie, Spatial organization of RNA polymerase II inside a mammalian cell nucleus revealed by reflected light-sheet superresolution microscopy, *Proc. Natl. Acad. Sci. U. S. A.* 111 (2014) 681–686.
- [40] G.T. Dempsey, J.C. Vaughan, K.H. Chen, M. Bates, X. Zhuang, Evaluation of fluorophores for optimal performance in localization-based super-resolution imaging, *Nat. Methods.* 8 (2011) 1027–1036.
- [41] D. Sage, H. Kirshner, T. Pengo, N. Stuurman, J. Min, S. Manley, et al., Quantitative evaluation of software packages for single-molecule localization microscopy, *Nat. Methods.* 12 (2015) 717–724.
- [42] A.D. Edelstein, M.A. Tsuchida, N. Amodaj, H. Pinkard, R.D. Vale, N. Stuurman, Advanced methods of microscope control using  $\mu$ Manager software, *J Biol Methods.* 1 (2014). doi:10.14440/jbm.2014.36.
- [43] A. Sergé, N. Bertaux, H. Rigneault, D. Marguet, Dynamic multiple-target tracing to probe spatiotemporal cartography of cell membranes, *Nat. Methods.* 5 (2008) 687–694.
- [44] L.S. Churchman, J.A. Spudich, Single-molecule high-resolution colocalization of single probes, *Cold Spring Harb. Protoc.* 2012 (2012) 242–245.
- [45] L.S. Churchman, J.A. Spudich, Colocalization of fluorescent probes: accurate and precise registration with nanometer resolution, *Cold Spring Harb. Protoc.* 2012 (2012) 141–149.
- [46] F.P. Cordelières, S. Bolte, Chapter 21 - Experimenters' guide to colocalization studies:

Finding a way through indicators and quantifiers, in practice, in: J.C.W.A.T. Wittman (Ed.), *Methods in Cell Biology*, Academic Press, 2014: pp. 395–408.

- [47] E.M. Manders, J. Stap, G.J. Brakenhoff, R. van Driel, J.A. Aten, Dynamics of three-dimensional replication patterns during the S-phase, analysed by double labelling of DNA and confocal microscopy, *J. Cell Sci.* 103 (1992) 857–862.
- [48] U. Schnell, F. Dijk, K.A. Sjollema, B.N.G. Giepmans, Immunolabeling artifacts and the need for live-cell imaging, *Nat. Methods.* 9 (2012) 152–158.
- [49] D.R. Whelan, T.D.M. Bell, Image artifacts in Single Molecule Localization Microscopy: why optimization of sample preparation protocols matters, *Sci. Rep.* 5 (2015). doi:10.1038/srep07924.
- [50] D.R. Whelan, T.D.M. Bell, Correlative Synchrotron Fourier Transform Infrared Spectroscopy and Single Molecule Super Resolution Microscopy for the Detection of Composition and Ultrastructure Alterations in Single Cells, *ACS Chem. Biol.* 10 (2015) 2874–2883.